Korean J. Chem. Eng., 40(8), 1993-2003 (2023)
DOI: 10.1007/s11814-023-1478-z

pISSN: 0256-1115
eISSN: 1975-7220

Thortveitite phase manganese vanadate ($Mn_2V_2O_7$) for the removal of model organic pollutants

Venkatesan Jayaraman*,, Mathankumar Ganesan*, Alagiri Mani*,†, and Do-Heyoung Kim**,†**

*Department of Physics and Nanotechnology, SRM Institute of Science and Technology, Kattankulathur, 603203, Chennai, Tamil Nadu, India
**School of Chemical Engineering, Chonnam National University, 77 Yongbong-ro, Gwangju 61186, Korea
(*Received 22 February 2023 • Revised 16 April 2023 • Accepted 1 May 2023*)

Abstract−Photocatalysis is useful for the long-term goal of a pollution-free environment. However, the development of new photoactive materials with enhanced photoconversion efficiency remains a serious bottleneck. This study demonstrates the preparation of low-cost, nontoxic, rod-like β-$Mn_2V_2O_7$ using a simple, cost-effective fabrication method. The proposed photoactive material was characterized using several analytical techniques to determine its physiochemical properties, while its photocatalytic ability for the removal of organic pollutants under direct sunlight was also assessed. The prepared β-$Mn_2V_2O_7$ was found to efficiently remove both Rhodamine B and methylene blue from an aqueous solution. The photoinduced and ultra-sound-assisted catalytic reduction of 4-nitrophenol (4-NP) was also demonstrated. The hydrogen-evolved photocatalytic removal of 4-NP was evaluated with different amounts of ethanol as a scavenger, with 10% ethanol exhibiting optimal efficiency. The superior organic pollutant removal ability of the proposed material is ascribed to its high surface area, superior optical properties, and suitable band edges.

Keywords: 4-Nitrophenol, Solar Energy, Photo-reduction, β-$Mn_2V_2O_7$ Rod

INTRODUCTION

Solar energy has been harnessed for use in a range of promising technologies [1], including advanced oxidation as a means to oxidize refractory pollutants via the redox capability of highly active radicals in aqueous media. In this process, the removal of highly toxic organic pollutants requires the development of heterogeneous photocatalysts. However, most of the photocatalyst materials presented to date are unsuitable for industrial purposes, because they do not meet the essential criteria for photoactive materials [2], such as a sufficiently small bandgap energy, high catalytic activity, and strong band edge potential for highly efficient redox reactions. In addition, photocatalysts require a high quantum yield, a low electron-hole recombination rate, a high surface area, a suitable textural structure, and the ability to generate a large volume of reactive radicals [3-5].

Though industrial wastewater contains a range of organic pollutants, including aromatic compounds (e.g., phenols, toluene, and chlorobenzene), one of the primary targets of photocatalysis-based pollutant removal is commercial dye. More than 100,000 types of commercial dye are currently in use in various industries, including rhodamine B (RhB), methylene blue (MB), acid red, methyl orange, ethyl violet, crystal violet, and malachite green, and many of these dyes are not readily biodegradable. In addition, because they are highly water-soluble, they are difficult to detect at low concentrations. This is a serious problem because dyes can be harmful to the ecosystem. For example, organic dye molecules in the hydrosphere can limit the diffusion of sunlight while also having mutagenic, carcinogenic, and/or teratogenic effects on flora and fauna. These dyes also pose a health risk to humans, potentially harming internal organs and causing skin allergies [6,7]. In particular, MB is a heterocyclic dye that is widely used in industrial applications such as dyeing and printing textiles. MB creates serious environmental pollution due to its high toxicity and stability. Similarly, RhB is extensively used as a colorant in textiles and foodstuffs and as a tracer fluorescent, and similar concerns have been raised regarding its toxicity [8]. Another organic pollutant of serious concern is 4-nitrophenol (4-NP), which has been classified as a priority pollutant. Because it is a common raw material in insecticides, drugs, dyes, and fungicides, 4-NP is widely found in industrial waste and agricultural and hospital effluent. It can have a damaging effect on the central nervous system, liver, kidney, and blood of humans and other organisms, with exposure often accompanied by headaches, drowsiness, and nausea. The conversion of 4-NP into 4-aminophenol (4-AP) is an important process in industrial production and has attracted greater academic and technological attention due to its lower toxicity. 4-AP is an organic intermediate for the production of various organic compounds such as dyes, agrochemicals, antipyretic drugs, and pharmaceuticals. It is also employed as a wood stain and dyeing agent for fur and feathers.

Many organic and inorganic-based semiconducting photocatalytic materials have been reported in previous studies, including TiO_2 [8], CdS [9], and Bi_2WO_6 [9]. These monophasic materials are often modified in various ways to increase their photocatalytic efficiency over the full spectrum of solar light. However, the development of novel materials with higher removal efficiency for organic molecules is still required. Metal oxides containing vanadium (V)

†To whom correspondence should be addressed.
E-mail: alagirimani@gmail.com, kdhh@chonnam.ac.kr

are considered particularly promising for use in a range of energy conversion and storage applications, including Li-ion storage, supercapacitors, photoelectrodes, and photocatalysts [10]. Due to its various oxidation states and functional properties, a large number of V-based metal oxides with different phases have been produced, including $BiVO_4$ [11], $Bi_4V_2O_{11}$ [12], V_2O_5 [13], $Cu_2V_2O_7(OH)_2 \cdot 2H_2O$ [14], $Zn_2V_2O_7$ [15] and $Mn_2V_2O_7$ [16,17], for use in solar water splitting, organic pollutant removal, and flexible and non-flexible electrochemical energy storage and conversion devices.

In general, the combined use of materials with bandgap energies ranging between 0.9-2.0 eV is most suitable for light absorbers, because this range covers the full solar spectrum, thus leading to the generation of a sufficient number of charge carriers. In this respect, $Mn_2V_2O_7$ has attracted significant attention across a diverse range of fields because it has a bandgap energy of less than 2.0 eV and is highly stable under light illumination and in alkaline solutions. Other advantageous properties include its low toxicity, high abundance, economic feasibility, and high energy density. Therefore, $Mn_2V_2O_7$ demonstrates significant potential for the removal of organic pollutants from wastewater using photocatalyst systems. However, pure β-$Mn_2V_2O_7$ is difficult to fabricate, with α phases and Mn_2O_3 often present as secondary phases. Xia et al. [17] reported the large-scale synthesis of pure β-$Mn_2V_2O_7$ using hydrothermal and annealing processes without the use of a template. Their β-$Mn_2V_2O_7$ sample exhibited a good cycling ability of 760 mAh g^{-1} at 0.5 A g^{-1} over 120 cycles and a rate capability of 470 mAh g^{-1} at 2 A g^{-1} as an anode material for a Li-ion battery. Sambandam et al. [16] also successfully prepared $Mn_2V_2O_7$ with a simple, economically feasible method. The prepared material had a superior reversible capacity of 868 mAh g^{-1} at 500 mA g^{-1} even after 180 cycles as an anode in a Li-ion battery. The as-prepared sponge-like $Mn_2V_2O_7$ material continued to produce a capacity of about 200 mAh g^{-1} at ~6,000 mA g^{-1}, which demonstrated the higher rate capability of the material. Yan et al. [18] reported a computational and experimental investigation of $Mn_2V_2O_7$ as a solar light absorber for water splitting. They calculated that the material had a bandgap of about 1.7 eV (the near-infrared region), making it suitable for photocatalytic activity. In this material, each element was shown to play a unique role in its structural and electronic properties. Similarly, Zhou et al. [19] introduced a novel molten preparation technique for single-crystal $Mn_2V_2O_7$ using different inorganic chloride salts. The single-crystalline nature of the sample was confirmed using X-ray diffraction (XRD) and selected area electron diffraction (SAED) analysis.

These studies indicate that $Mn_2V_2O_7$ offers near-infrared bandgap absorption under solar light illumination. The robust hybridization between the Mn 3d and O 2p electronic states leads to the formation of the valence band maximum with a higher redox potential. On the other hand, the V 3d electronic states may lead to the formation of the conduction band maximum. In the present study, we present the successful production of novel monophasic β-$Mn_2V_2O_7$ rods using a facile calcination and hydrothermal fabrication method. The properties of the β-$Mn_2V_2O_7$ crystal phase were characterized using a variety of methods to determine its functional properties, and the photocatalytic removal of MB and RhB as model organic pollutants was assessed. Finally, the effectiveness of the prepared photocatalyst for 4-NP reduction in an aqueous solution was also tested.

MATERIALS AND METHODS

All chemicals purchased for use in the experiments were of analytical grade, including manganese (II) carbonate ($MnCO_3$; Sigma Aldrich), ammonium metavanadate (NH_4VO_3; SRL India), nitric acid (HNO_3), sodium hydroxide (NaOH) pellets (SRL India), ethanol (C_2H_5OH; China), acetone (C_3H_6O), 4-NP (SRL), and sodium borohydride (SRL India).

1. Preparation of β-$Mn_2V_2O_7$

Novel rod-like β-$Mn_2V_2O_7$ was prepared using a simple hydrothermal and calcination process. In the typical synthesis route, 0.2 mol $MnCO_3$ was dissolved in distilled water (40 mL) and HNO_3 (2 mL) to produce solution A. Solution B was prepared by dissolving 0.2 mol NH_4VO_3 in distilled water (40 mL) and HNO_3 (2 mL). After producing a transparent solution, the two solutions were mixed by adding solution A to solution B dropwise. The mixture was then stirred vigorously for 2 h with the addition of 10 mL of 4 mol NaOH solution. The resulting colloid-like solution was then transferred into a Teflon-lined autoclave and sealed, before being heated to 180 °C for 24 h. The autoclave was subsequently rapidly cooled to room temperature using tap water. The collected precipitate was washed with ethanol and distilled water several times to remove the unreacted material. The obtained sample was then dried at 80 °C and calcinated at 550 °C for 8 h, before being ground to a fine powder for further characterization.

2. Characterization Techniques

Structural analysis was conducted using a PANalytical instrument (Netherlands) with a scanning range of 10 to 80°. The surface morphology of the samples was assessed using a high-resolution scanning electron microscope (HRSEM; FEI Quanta FEG 200) equipped with a Bruker EDS attachment. High-resolution transmission electron microscopy (HRTEM) measurements were carried out with a JEOL microscope (Japan). The surface chemical states of the elements were analyzed using X-ray photoelectron spectroscopy (XPS; Physical Electronics) at a binding energy of 0 to 1,100 eV. The vibrational spectrum of the samples was studied using a confocal Raman microscope (Horiba, France) at an excitation wavelength of 532 nm and a wavenumber range of 100-2,000 cm^{-1}. Fourier-transform infrared spectroscopy (FTIR) was conducted from 400 to 4,000 cm^{-1} in ATR mode using an IRTracer-100 spectrometer (Shimadzu). The optical properties of the samples were analyzed using a UV-3600 Plus UV-Vis-NIR spectrometer (Shimadzu) over a scanning range of 200-800 nm.

3. Photocatalytic Activity of the Material

The photocatalytic removal activity for the organic pollutants MB and RhB was measured with a standard procedure; the experimental details are provided in Section 3.10. The photocatalytic and ultrasound-assisted catalytic reduction ability of β-$Mn_2V_2O_7$ for 4-NP was analyzed using 100 mL of 10 ppm 4-NP solution prepared in distilled water. First, 5 mL of freshly prepared $NaBH_4$ solution (1 mg mL^{-1}) was added to the 4-NP solution as a reductant. Following this, 50 mg of the prepared catalyst was added to the solution and placed in direct sunlight between 11 am and 3 pm with

minimal fluctuation in the solar intensity, which was measured using a lux meter (average=43,000 lux). During photodegradation, 3-mL aliquots of the solution were collected at fixed time intervals. The catalyst powder was removed by centrifugation. Its absorbance was analyzed using a UV-Vis instrument in the 200-600 nm region. The temperature of the photo-reaction solution was constantly monitored to hold it at around 34 °C. The 4-NP reduction reaction was also assisted with ultrasound by placing the catalyst-containing solution in an ultrasonicator, and its absorbance was monitored.

For the hydrogen-evolved photo-reduction reaction, a 10 ppm 4-NP solution was prepared in distilled water with 5, 10, or 15% ethanol to act as a scavenger. Following this, 0.2 mL of freshly prepared $NaBH_4$ solution (1 mg mL^{-1}) was added to 100 ml of the 4-NP/ethanol mixture as a reductant. The solutions were then used for the degradation reaction under the same experimental conditions used for the reduction of 4-NP.

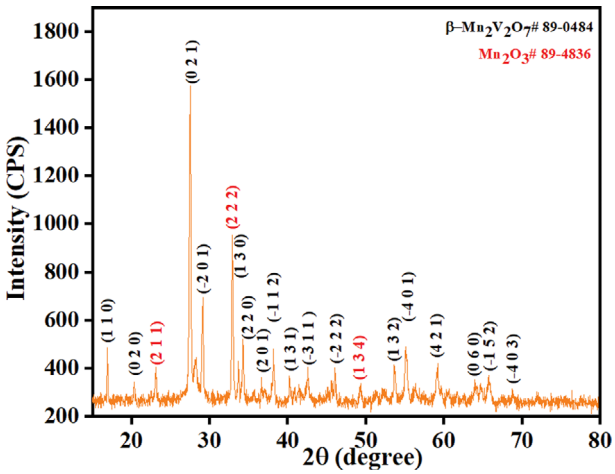

Fig. 1. X-ray diffraction patterns for β-$Mn_2V_2O_7$.

RESULT AND DISCUSSION

1. XRD Analysis

Powder XRD patterns were used to examine the structure and phase purity of the final product from the hydrothermal and calcination processes (Fig. 1). Distinctive sharp diffraction peaks were observed at 2θ values of 16.96, 20.34, 27.53, 29.18, 33.71, 34.28, 36.64, 37.99, 40.22, 42.6, 46.06, 53.63, 54.99, 59.22, 63.96, 65.6, and

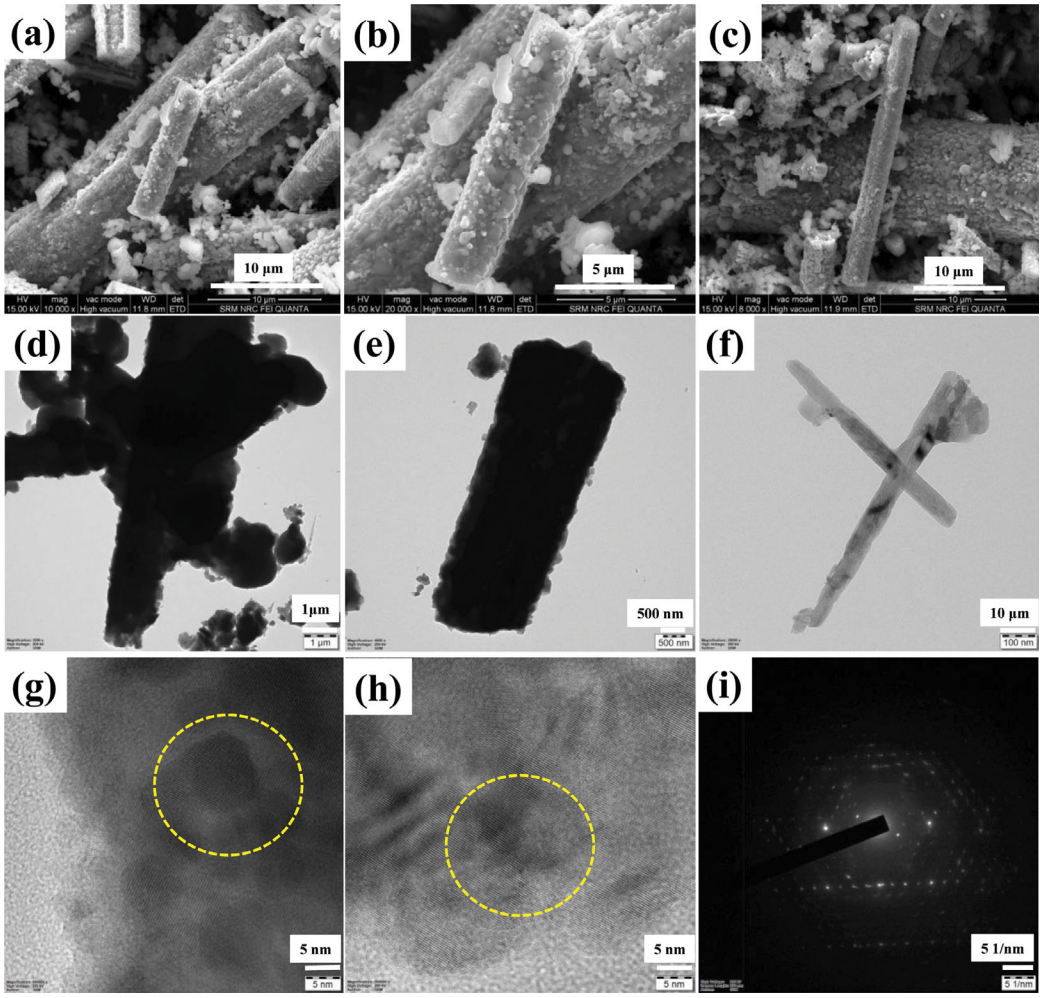

Fig. 2. (a)-(c) FESEM images, (d)-(f) TEM images, (g), (h) HRTEM images, and (i) SAED patterns for β-$Mn_2V_2O_7$.

72.0°, which were indexed to the (1 1 0), (0 2 0), (0 2 1), (−2 0 1), (1 3 0), (2 2 0), (2 0 1), (−1 1 2), (1 3 1), (−3 1 1), (−2 2 2), (1 3 2), (−4 0 1), (−4 2 1), (0 6 0), (−1 5 2), and (−4 0 3) crystallographic planes of β-$Mn_2V_2O_7$, respectively. The characteristic diffraction peaks of Mn_2O_3 as a secondary phase were also observed at 2θ values of 23.12, 32.96, and 49.36°, which were assigned to the (2 1 1), (2 2 2), and (1 3 4) planes, respectively. Similar results have been reported for structural changes in Mn-V-O materials [17,19-22]. The XRD results thus confirmed the successful formation of $Mn_2V_2O_7$.

2. Morphological and Elemental Analysis

The surface morphology of β-$Mn_2V_2O_7$ was investigated using FESEM analysis (Fig. 2(a)-(c)). The β-$Mn_2V_2O_7$ samples consisted of micro-rods with similar morphologies, illustrating the purity of the sample [23]. The size of the individual rods was measured to be ~2.2 µm. The morphology of the obtained β-$Mn_2V_2O_7$ was also investigated using TEM and HRTEM analysis (Fig. 2(d)-(f)). The resulting images revealed a β-$Mn_2V_2O_7$ phase consisting of micro-rod-like structures made up of nanoparticles, which was in agreement with the FESEM analysis. HRTEM images were also used to measure the lattice fringe of β-$Mn_2V_2O_7$, which was found to be 0.32 nm, roughly in accordance with the (0 2 1) plane of the catalyst (Fig. 2(g), (h)). The SAED pattern of the β-$Mn_2V_2O_7$ is presented in Fig. 2(i), which was indexed to monoclinic phases. Subsequently, the elements presented in the β-$Mn_2V_2O_7$ powder sample were identified using EDS analysis (Fig. 3), showing that Mn, V, and O were uniformly distributed within the obtained material (Table 1).

3. Raman and FTIR Analysis

To verify the phase formation and purity of the catalyst using its vibrational modes, the prepared sample was subjected to Raman spectral analysis (Fig. 4(a)). Six active Raman modes were identified, with one strong peak located at 837 cm^{-1} and the other peaks at about 121, 154, 255, 362, and 484 cm^{-1}. In Fig. 4, the intense peak at 837 cm^{-1} is related to the [VO_4] stretching vibrations, while the peaks at 484 and 362 cm^{-1} are attributed to the symmetric scaling mode and [VO_4] bending vibrations, respectively. The lower frequency peaks at 121, 154, and 255 cm^{-1} are associated with crystal lattice translations and rotational modes, respectively [15,23]. The

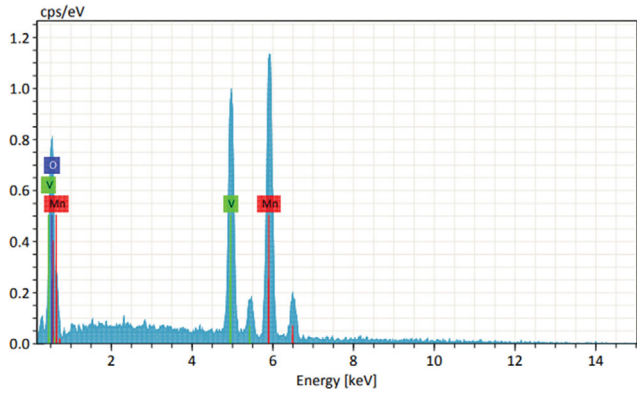

Fig. 3. EDS analysis of β-$Mn_2V_2O_7$.

Table 1. Elemental composition of the sample

Element	Mass %	Atom %
Mn	47.49	46.52
V	24.83	26.23
O	8.10	27.25

observed Raman peaks confirm the successful formation of β-$Mn_2V_2O_7$ without secondary phases. The FTIR spectrum for the prepared β-$Mn_2V_2O_7$ sample for the 400-4,000 cm^{-1} region is presented in Fig. 4(b). In general, metal oxides exhibit characteristic vibrational properties in the fingerprint region of transmittance [3]. The obtained spectrum exhibits a broad vibration from 1,600 to 3,100 cm^{-1}, which is ascribed to the O-H stretching vibrations of the hydroxyl groups. The bands observed at a lower wavenumber range are attributed to octahedral MnO_6 and tetrahedral VO_4 in the crystal network. The strong band at 918 cm^{-1} appears to be the symmetric stretching mode of v1 (VO_3). The bands at 800 and 750 cm^{-1} correspond to the anti-symmetric stretching of v3 (VO_3). The lower wavenumber bands at 565 and 509 cm^{-1} may be due to the V-O-V units [15,23].

4. XPS Analysis

The as-synthesized β-$Mn_2V_2O_7$ was subjected to XPS analysis

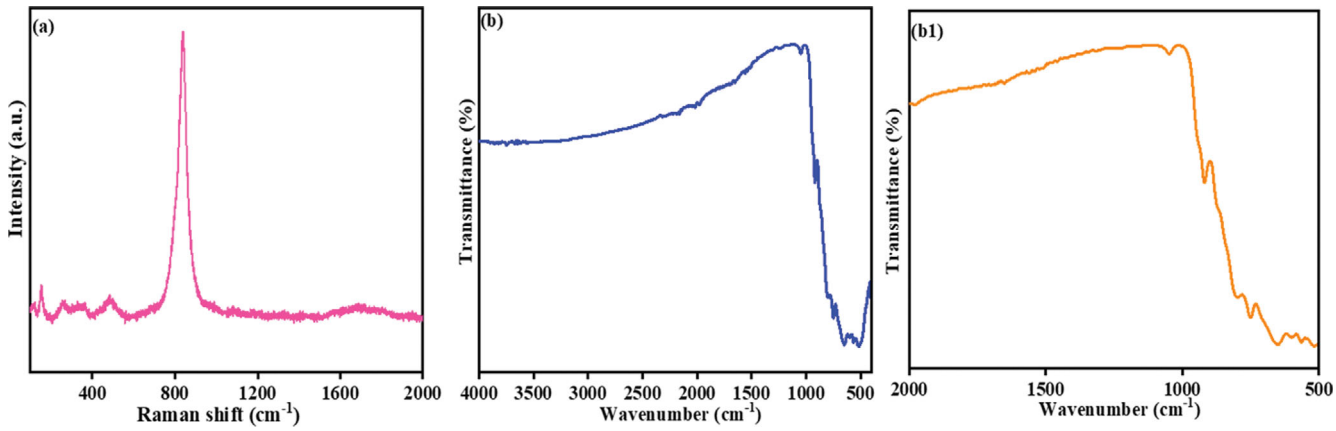

Fig. 4. (a) Raman and (b), (b1) FTIR spectra for β-$Mn_2V_2O_7$.

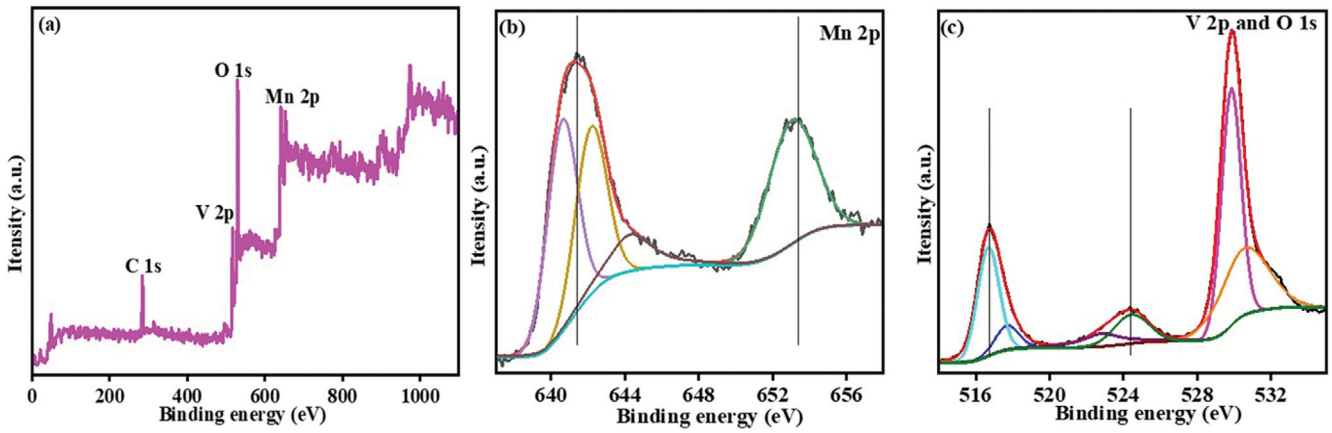

Fig. 5. XPS analysis (a) a survey scan of $Mn_2V_2O_7$, (b) Mn 2p, and (c) V 2p and O 1s.

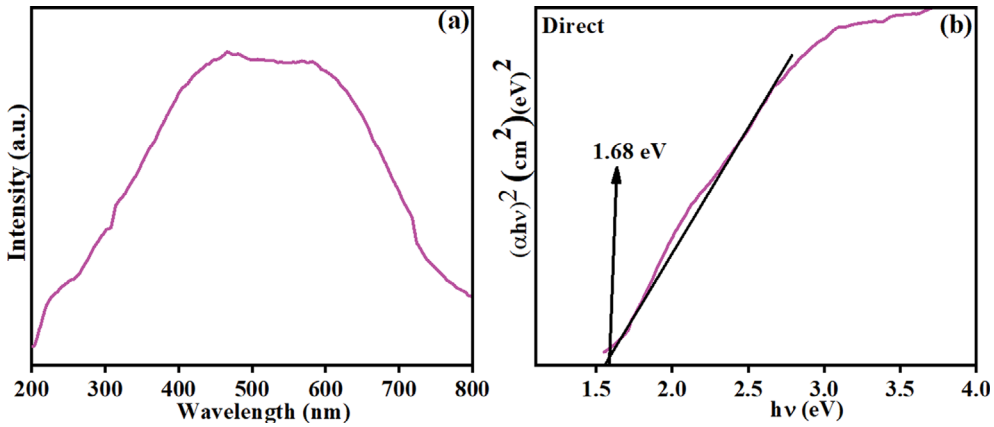

Fig. 6. Optical properties of β-$Mn_2V_2O_7$. (a) UV-Vis near-infrared spectrum. (b) Tauc plot.

to verify its composition and surface chemical state. The survey scan spectrum for β-$Mn_2V_2O_7$ is presented in Fig. 5(a), indicating the presence of Mn 2p, V 2p, and O 1s in the material. The core-level Mn 2p, V 2p, and O 1s spectra were deconvoluted, and the results are presented in Fig. 5(b), (c). The high-resolution Mn 2p spectrum contains two peaks at around 641.32 and 653.24 eV with a spin-orbital splitting energy of about ΔE=11.92 eV, which are related to the $2p_{3/2}$ and $2p_{1/2}$ states, respectively. The deconvoluted spectra reveal the three-valence state of Mn $2p_{3/2}$, as indicated by the binding energies of 640.7, 642.2, and 644.4 eV. These observed shoulder peaks are attributed to the +2, +3, and +4 valence states of Mn $2p_{3/2}$, respectively [16,17]. Similarly, the V core spectrum reveals valence states of +4 and +5 with broad peak splitting at 516.75 (V $2p_{3/2}$) and 524.39 eV (V $2p_{1/2}$). These +4 and +5 valence states for V 2p were determined from the fitted peak values (516.6, 517.33, and 517.71 eV from 516.75 eV and 522.85 and 524.58 from 524.39 eV) [4,13,14,16,17]. The O 1s spectrum reveals two peaks at around 529.8 and 530.7 eV with a broad peak centered at 529.89 eV. The two peaks are attributed to the lattice and surface-adsorbed or dangling bonds of O, respectively [4,13,14,16,17]. These XPS results confirm the presence of Mn (+2, +3, +4), V (+4, +5), and O (−2) oxidation states, which is in accordance with the XRD and Raman analyses, thus verifying the formation of β-$Mn_2V_2O_7$.

5. Optical Properties of $Mn_2V_2O_7$

The light absorption properties of the as-obtained $Mn_2V_2O_7$ were examined using a UV-Vis-NIR DRS spectrometer (Fig. 6(a)). β-$Mn_2V_2O_7$ exhibits strong absorption from the pure visible to the near-infrared region, while the absorption in the UV region is very weak, and a strong absorption edge is observed at around 635 nm. The bandgap energy of β-$Mn_2V_2O_7$ was also calculated using a Tauc plot with the direct transition of charge carriers in the bands of the semiconductor [20]. The plot of $(\alpha h\nu)^2$ against hν is presented in Fig. 6(b). The bandgap energy for β-$Mn_2V_2O_7$ was calculated to be around 1.68 eV, which closely corresponded with the theoretical and experimental results from previous studies [20], though with a slight shift toward a lower value, possibly due to the presence of Mn_2O_3 as a secondary phase. A sufficiently high band edge potential is required for photoresponsive and catalytic reactions in photocatalysis systems. The conduction and valence bands of the as-prepared β-$Mn_2V_2O_7$ with respect to a normal hydrogen electrode were estimated using calculations reported by Butler and Ginley and Xu and Schoonen as follows [20]:

$$E_{VB,CB}=E_0+(\chi^2\mathrm{Mn}\,\chi^2\mathrm{V}\chi^7\mathrm{O})^{1/11}\pm E_g/2$$

where E_0 is −4.5 eV, which is the difference between a normal hydrogen electrode and a vacuum, and χ is the Mulliken electroneg-

ativity of the atomic constituents of the material. The electronegativity of β-$Mn_2V_2O_7$ was calculated using the standard method to be about 5.7875 V [20], while the conduction band and valence band maxima for β-$Mn_2V_2O_7$ were calculated with respect to a normal hydrogen electrode and found to be 0.43 and 2.13 V, respectively. These estimated values are in close agreement with those from previous reports, and they indicate that the proposed material has a strong redox ability for the removal of organic molecules.

6. Texture Analysis

The Brunauer-Emmett-Teller (BET) N_2 adsorption-desorption process was used to evaluate the specific surface area and average pore size distribution of β-$Mn_2V_2O_7$. The observed N_2 adsorption-desorption graph is displayed in Fig. 7(a)-(b). The as-prepared β-$Mn_2V_2O_7$ exhibits H_3-type hysteresis and a mesoporous structure, with a specific surface area of about 10.115 $m^2\ g^{-1}$ which is much higher than values reported elsewhere. The average pore diameter and volume were estimated using BJH desorption and are summarized in Table 2 alongside previously reported materials for comparison. These results indicate that β-$Mn_2V_2O_7$ may have a higher number of catalytic sites due to its higher surface area, thus leading to higher photoactivity.

7. Formation Mechanisms for β-$Mn_2V_2O_7$

The reaction mechanisms responsible for the formation of β-$Mn_2V_2O_7$ were also determined. To produce β-$Mn_2V_2O_7$, $MnCO_3$ was dissolved in a mixture of distilled water and HNO_3. Mn^{2+} ions were subsequently produced from the $MnCO_3$ precursor with the combination of the solvents according to the following equation:

$$MnCO_3 \rightarrow Mn^{2+} + CO_3^{2-}$$

NH_4VO_3 powder was dissolved in a mixture of distilled water and HNO_3, forming V^{5+} ions and other byproducts:

$$2Mn^{2+} + 2CO_3^{2-} + NH_4VO_3 \rightarrow Mn_2V_2O_7 + (NH_4)_2CO_3 + CO_2$$

Manganese hydroxide and manganese vanadium hydroxide were formed with the addition of NaOH to the mixture of the ionic Mn^{2+} and V^{5+} solutions. Hydrothermal treatment consequently led to the formation of β-$Mn_2V_2O_7$ and Mn_2O_3 with impurities. As reported in previous studies, the addition of NaOH did not lead to any morphological changes but led to the formation of Mn_2O_3. After hydrothermal treatment, the Teflon-lined autoclave was rapidly cooled to room temperature by immersing it in tap water, which may have led to the aggregation of particles and the formation of rod-like structures with a significantly higher surface area [24].

8. Photocatalytic Activity

The photocatalytic removal of MB and RhB as target contaminants was tested for the as-prepared β-$Mn_2V_2O_7$ under direct sunlight. In this experiment, 50 mL of a 10 ppm dye solution was mixed with 50 mg of the as-prepared β-$Mn_2V_2O_7$ catalyst. Before the experimental analysis, adsorption-desorption and photolysis experiments were conducted to confirm the stability of the catalyst and dye solutions. The resulting adsorption and photolysis effects were ignored in the spectral measurements. The RhB and MB solutions containing the catalyst were placed under direct sunlight, with aliquots collected at specific time intervals and analyzed using a

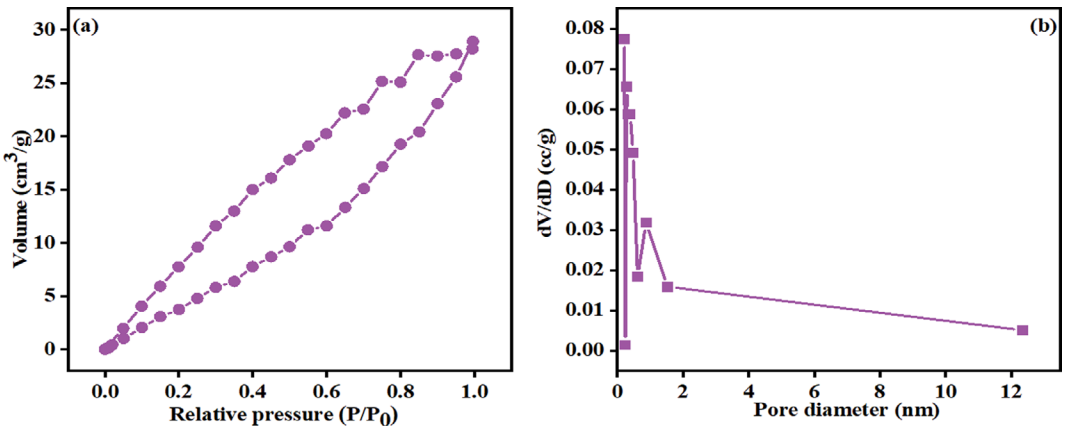

Fig. 7. Textural analysis of β-$Mn_2V_2O_7$.

Table 2. Surface area and BET results for β-$Mn_2V_2O_7$

Sample	Specific surface area $m^2\ g^{-1}$	Pore volume	Average pore radius	Ref.
$Mn_2V_2O_7$ and MnV_2O_6	6.6	0.0424	25.302 nm	[32]
$Mn_2V_2O_7$	1.01	-	-	[33]
β-$Mn_2V_2O_7$	7.7	-	-	[17]
α-$Zn_2V_2O_7$	45.28	0.51	30.09 nm	[15]
$Mn_2V_2O_7$	16.5	-	3.9 nm	[34]
β-$Mn_2V_2O_7$	10.115	0.047	15.260 Å	This work

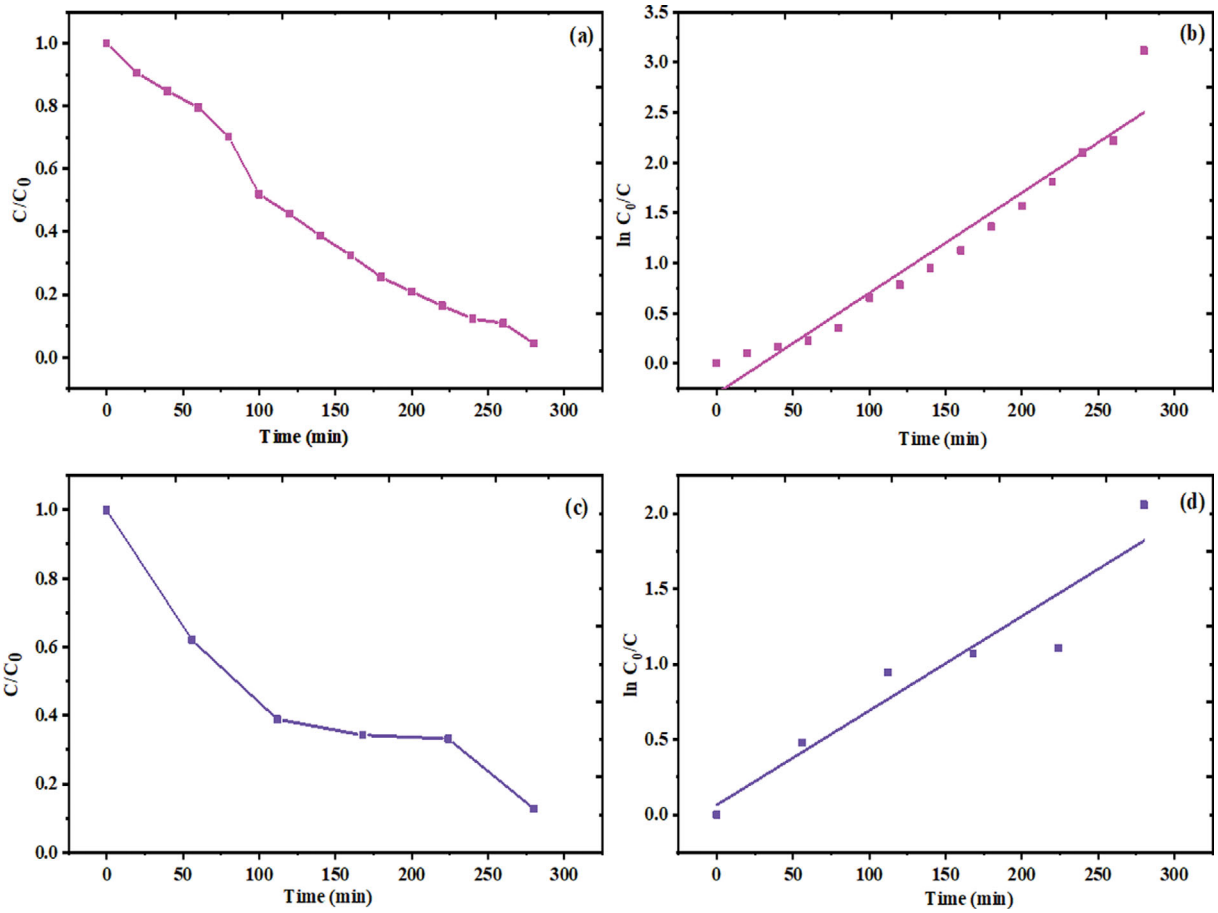

Fig. 8. (a), (c) Concentration of RhB and MB. (b), (d) Reaction kinetics for RhB and MB.

Table 3. Degradation profile for the dye solutions using β-$Mn_2V_2O_7$

Sample name	MB			RhB		
	R^2	K (min^{-1})	Efficiency %	R^2	K (min^{-1})	Efficiency %
$Mn_2V_2O_7$	0.9032	0.00626	87.23	0.944	0.00999	95.55

UV-Vis instrument. The spectral changes and the λ_{max} of the samples were measured, with C/C_0 plotted to assess the degradation efficiency of $Mn_2V_2O_7$ (Fig. 8(a), (c)). In general, the concentration of the dye solutions containing β-$Mn_2V_2O_7$ gradually declined with increasing irradiation time, with a degradation efficiency for RhB and MB over 280 min of around 95.55 and 87.23%, respectively. This degradation activity of the β-$Mn_2V_2O_7$ catalyst against organic pollutants was ascribed to its visible-light-responsive nature and high surface area. To quantify the degradation rate and degradation process for the dye solutions, the degradation spectra for β-$Mn_2V_2O_7$ were investigated using the Langmuir-Hinshelwood model. The degradation spectra were fitted to the pseudo-first-order kinetic reaction model and the results are summarized in Table 3, and the fitted graphs for RhB and MB are presented in Fig. 8(b), (d). Both RhB and MB exhibit a good degradation rate. The proposed process of radical production and subsequent degradation of the dyes using β-$Mn_2V_2O_7$ is schematically illustrated in Fig. 9(a). The stability of a photocatalyst is very important for industrial applications. Therefore, used β-$Mn_2V_2O_7$ was subjected to XRD analysis, and the results were compared to the pristine material (Fig. 9b). The results show that β-$Mn_2V_2O_7$ remains unchanged after the degradation process in direct sunlight. These experimental results collectively indicate that β-$Mn_2V_2O_7$ has good efficiency, recyclability, and stability.

9. Sunlight- and Ultrasound-assisted 4-NP Reduction

Direct sunlight- and ultrasound-assisted catalytic reduction of 4-NP using β-$Mn_2V_2O_7$ was also assessed. Because the reduction reaction of phenolic compounds occurs on the surface of a catalyst, its surface area and catalytic sites play a vital role in this reaction. The adsorption capacity of β-$Mn_2V_2O_7$ was monitored in the dark under stirring conditions with a 4-NP solution containing no other additives. An adsorption-desorption equilibrium between β-$Mn_2V_2O_7$ and 4-NP was achieved, and the degree of adsorption was negligible. The pure 4-NP solution had a λ_{max} of around 316 nm and was bright yellow, and the absorbance intensity increased with the addition of $NaBH_4$. λ_{max} was found to be 400 nm for the

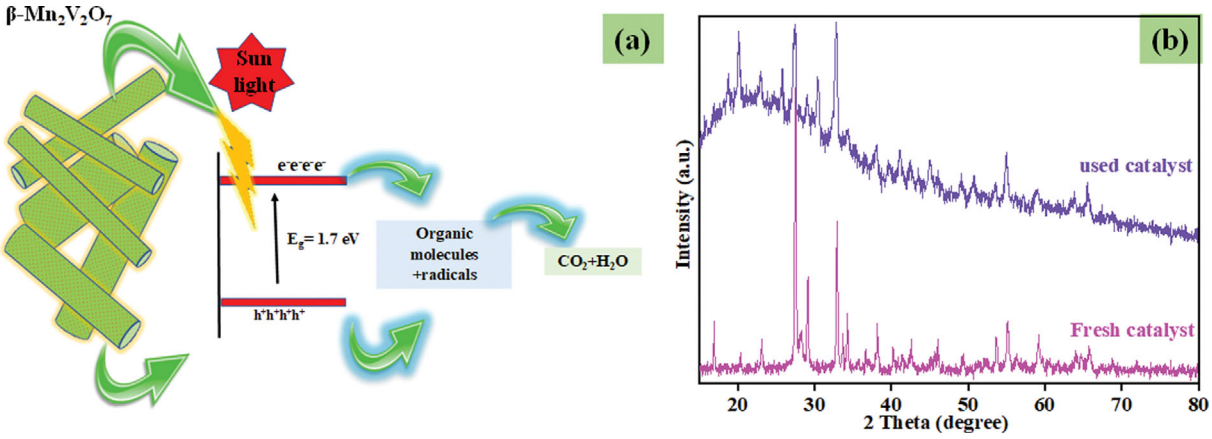

Fig. 9. (a) Schematic overview of the degradation mechanisms for organic molecules. (b) XRD patterns for the used and fresh catalyst.

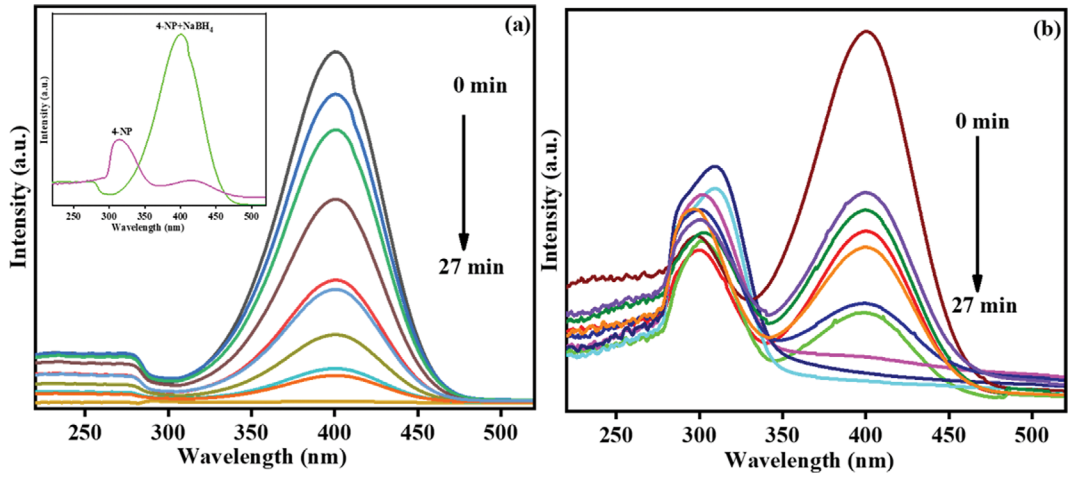

Fig. 10. Spectral changes in 4-NP due to β-$Mn_2V_2O_7$ under (a) sunlight and (b) ultrasound.

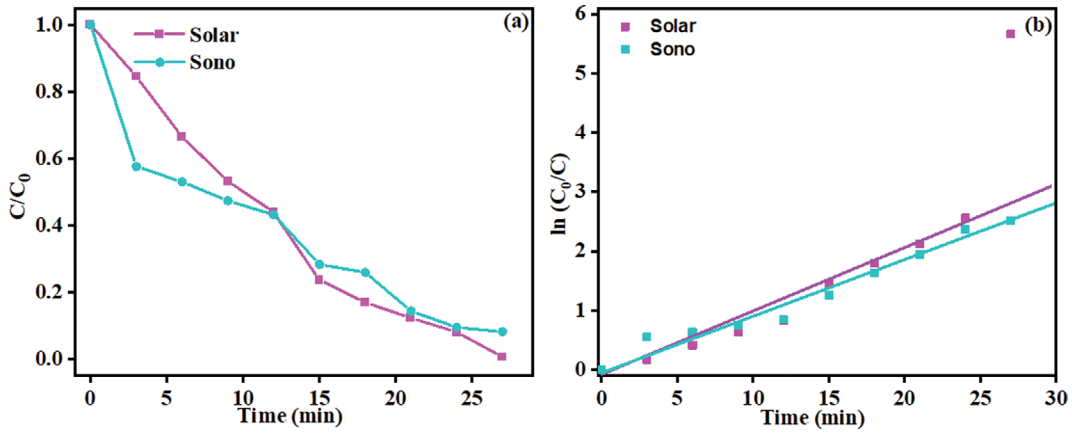

Fig. 11. (a) 4-NP concentration over time and (b) the corresponding kinetics plot for β-$Mn_2V_2O_7$.

light-yellow solution of 4-NP. This observed shift in the absorbance region indicated the conversion of 4-NP into 4-nitrophenolate ions. The conversion efficiency was calculated using the absorbance values at 400 nm. The sunlight- and ultrasound-assisted reduction processes were both more highly efficient than previous reports. The resultant absorbance intensity in relation to the wavelength for the photocatalytic and ultrasound-assisted conversion of 4-NP is presented in Fig. 10. The inset shows the spectral shift in the absorbance with the addition of $NaBH_4$. For the sunlight-assisted photoreduction reaction, the spectra change vertically without any sign of the conversion of 4-NP into 4-AP. In contrast, the ultrasonic catalytic conversion process exhibits an increase in the absorbance

intensity at around 300 nm. This indicates the formation of the comparatively less toxic 4-AP, which is colorless. These differences in the absorbance spectra could be attributed to different conversion pathways. The efficiency of β-$Mn_2V_2O_7$ for the conversion of 4-NP was calculated based on Fig. 11(a) and found to be around 99.6 and 91.0% for sunlight- and ultrasound-assisted catalytic reduction over 27 min. The reaction rate constant and the kinetics for these processes were also calculated. The kinetics for the reaction conversion from 4-NP to 4-AP is presented in Fig. 11(b). The following equation was used to calculate the rate of the reaction:

$$-\ln(C_0/C_t)=K_{app}\,t,$$

where C_0 and C_t denote the initial concentration of the 4-NP reaction solution and the concentration at time t, respectively, while K_{app} represents the reaction rate constant. According to the Langmuir-Hinshelwood model, the fitted reaction curves for both the sunlight- and ultrasound-assisted conversion reduction reactions followed pseudo-first-order kinetics, from which the reaction constant was calculated to be 0.0973 and 0.090 min^{-1}, respectively. Similarly, the R^2 value should be above 0.89 for a first-order-kinetic reaction; it was found to be 0.958 under sunlight and 0.954 with ultrasonic assistance. The prepared β-$Mn_2V_2O_7$ thus had strong reduction activity against 4-NP, with an efficiency that was considerably higher than or comparable with previously reported materials.

10. Hydrogen-evolved Photo-catalytic Reduction

Ethanol and $NaBH_4$ were subsequently incorporated into the reduction reaction process as a hole scavenger and reducing agent, respectively. These reagents were selected for their combined reduction and degradation pathways (among many available hole scavengers such as $NaSO_4$, formic acid, and EDTA) [25]. Bekena et al. and Abdullah et al. have previously reported the use of $NaBH_4$ in the photocatalytic reduction of para-nitrophenol, and ethanol has been used as a hole scavenger in photo-degradation [25,26]. The 4-NP conversion efficiency with ethanol is summarized in Fig. 12. The photoreaction between 4-NP and $Mn_2V_2O_7$ with 5% ethanol and $NaBH_4$ under direct sunlight led to the generation of highly active H^+ ions, which were responsible for the degradation of the 4-NP (Fig. 12(a)). However, the reaction rate was slow due to the rapid recombination of the carriers and the conversion of H^+ ions into hydrogen by the available electrons in the conduction band of the catalyst [25,26]. The reaction between $Mn_2V_2O_7$ and 4-NP with 10% ethanol and $NaBH_4$ under sunlight led to the initial reduction of 4-NP to 4-AP and other byproducts, which is indicated by the observed changes in color and the shift from a λ_{max} of 400 nm and 316 nm to 298 nm. The reaction ended with the complete reduction and degradation of 4-NP, as confirmed by the UV-Vis spectral changes after 24 min. The reaction between $Mn_2V_2O_7$ and 4-NP with 15% ethanol and $NaBH_4$ also led to reduction and degradation, though with a lower generation of H^+ ions via the excited carriers from the $Mn_2V_2O_7$. The changes in the absorbance peak intensity in the 300-400 nm spectral regions and the color transformation from strong yellow to colorless are attributed to the reduction of 4-NP to 4-AP and degradation into other chemical byproducts [27-29]. In all three reactions, the peak intensity at around 316 nm remained steady with the addition of ethanol and $NaBH_4$, representing the unreacted 4-NP solution.

The reaction efficiency and rate for $Mn_2V_2O_7$ were calculated using Fig. 12(b), which plots the concentration changes at around 400 nm over time. The calculated 4-NP removal efficiency for β-$Mn_2V_2O_7$ under sunlight with $NaBH_4$ and 5%, 10%, or 15% ethanol was 52%, 87%, and 81%, respectively, which was the result of a combination of reduction and degradation reactions. The reaction rate constant for β-$Mn_2V_2O_7$ under sunlight with $NaBH_4$ and 5%, 10%, or 15% ethanol was 0.0318, 0.076, and 0.0605 min^{-1}, respectively, with a corresponding R^2 of 0.098, 0.096, and 0.097, respectively. These results indicate that the reactions followed pseudo-first-order kinetics. The observed reaction rate constants depend on the initial concentration of the $NaBH_4$ and 4-NP solution. The addition of a high level of $NaBH_4$ solution will cause the material surface [30]. In general, the efficiency of 4-NP removal is directly connected with the adsorption ability of the catalyst material and its surface area [31]. The obtained results are compared with previously available materials in Table 4.

11. Possible Reaction Mechanisms for the Removal of 4-NP

The possible 4-NP reduction mechanisms for β-$Mn_2V_2O_7$ with the assistance of $NaBH_4$ as a reductant and either sunlight or ultra-

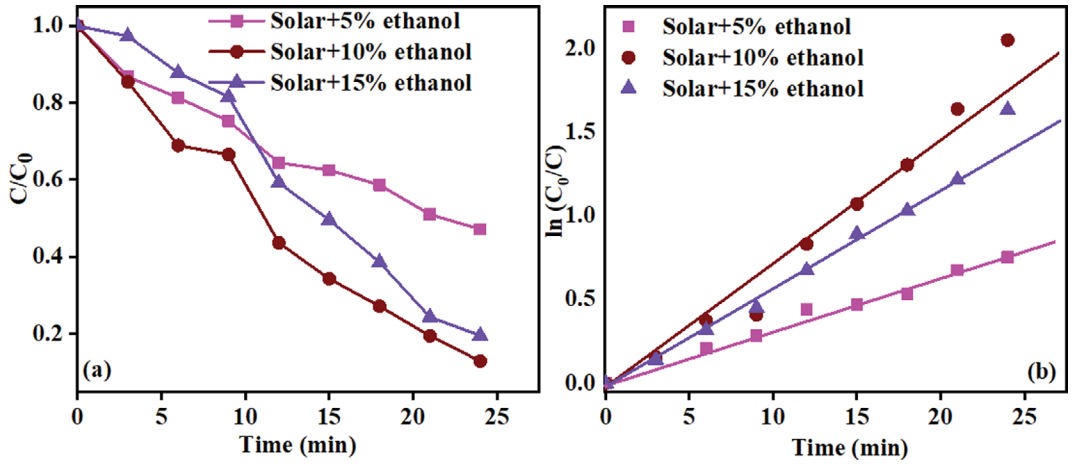

Fig. 12. (a) 4-NP concentration over time for the hydrogen evolution reaction and (b) the corresponding kinetics plot for β-$Mn_2V_2O_7$.

Table 4. Photocatalytic removal of 4-NP by various catalysts

Sample name	Efficiency	Kinetics	References
Co@N-CNT		0.62 min^{-1}	[35]
Cu_2O/Fe_3O_4@C/Cu		1.2544	[36]
g-C_3N_4@HPC-700		0.120 min^{-1}	[37]
CuS/ZnS@PVP	100%		[38]
NiS_2@NSC		0.0550 S^{-1}	[39]
10% ethanol $Mn_2V_2O_7$	87%	0.076	This study

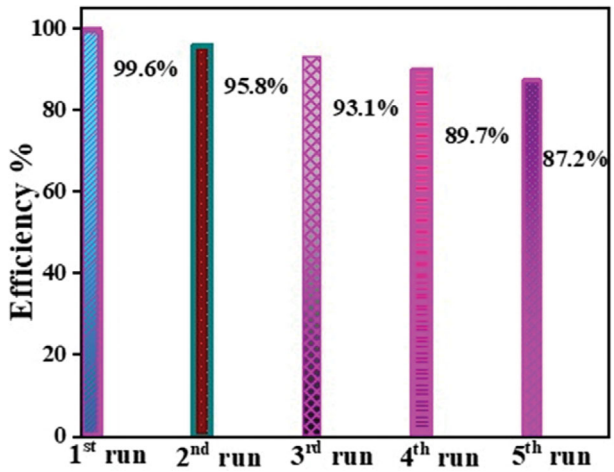

Fig. 13. Stability analysis of the catalyst.

sound were also elucidated. During the reduction reaction, 4-NP and BH_4^- ions adhered to the surface of the β-$Mn_2V_2O_7$ rods. The illumination of direct sunlight and ultrasound vibrations generated electrons, which were excited in the conduction band of β-$Mn_2V_2O_7$. There was no direct experimental evidence for a two-channel reduction reaction for 4-NP using β-$Mn_2V_2O_7$. However, previous studies have outlined potential two-channel reduction reactions [25,26].

12. Stability Analysis

The recyclability and stability of a catalyst are important for its potential industrial applications. Therefore, the reduction of 4-NP under sunlight using β-$Mn_2V_2O_7$ was also monitored under cycling tests (Fig. 13). It was found that the proposed catalyst retained its efficiency after several cycles with only a slight decrease from 99.6% to 87.2%. The incomplete recovery of the catalyst and potential damage due to the addition of $NaBH_4$ may have led to this decrease in the reduction activity of β-$Mn_2V_2O_7$. However, these experimental results collectively indicate that β-$Mn_2V_2O_7$ has good efficiency, recyclability, and stability.

CONCLUSION

The present study focused on the preparation of a β-$Mn_2V_2O_7$ catalyst and the subsequent analysis of its photocatalytic degradation of RhB, MB, and 4-NP. The prepared β-$Mn_2V_2O_7$ catalyst was also characterized using FESEM, HRTEM, XRD, UV-Vis, FTIR, and BET analysis. Higher photocatalytic activity was observed due to a combination of a high surface area and excellent electron-hole separation. The obtained results indicate that β-$Mn_2V_2O_7$ has suitable physicochemical properties for the effective photodegradation of dye molecules under direct sunlight. However, further modifications and testing are needed for monophasic β-$Mn_2V_2O_7$ to improve its degradation of organic pollutants.

ACKNOWLEDGEMENTS

This research was partially supported by the Basic Science Research Capacity Enhancement Project through a Korea Basic Science Institute (National Research Facilities and Equipment Center) grant funded by the Ministry of Education (Grant No. 2019R1A6C1010024). We acknowledge the HRTEM Facility at SRMIST set up with support from the MNRE (Project No. 31/03/2014-15/PVSE-R&D), the Government of India, the SRM Institute of Science and Technology for providing the Micro-Raman Facility, and SRMIST for the high-resolution scanning electron microscope (HR-SEM) facility. We acknowledge the Nanotechnology Research Centre (NRC) at SRMIST for providing the research facilities.

REFERENCES

1. A. Kudo and Y. Miseki, *Chem. Soc. Rev.*, **38**, 253 (2009).
2. Y. Yang, G. Zeng, D. Huang, C. Zhang, D. He, C. Zhou, W. Wang, W. Xiong, B. Song and H. Yi, *Small*, **16**, 2001634 (2020).
3. K. Chaudhary, N. Shaheen, S. Zulfiqar, M. I. Sarwar, M. Suleman, P. O. Agboola, I. Shakir and M. F. Warsi, *Synth. Met.*, **269**, 116526 (2020).
4. V. Jayaraman, M. Chinnan, P. Alagarsamy and A. Mani, *Mater. Sci. Semicond. Process.*, **124**, 105611 (2021).
5. C.-C. Wang, J.-R. Li, X.-L. Lv, Y.-Q. Zhang and G. Guo, *Energy Environ. Sci.*, **7**, 2831 (2014).
6. R. Gusain, K. Gupta, P. Joshi and O. P. Khatri, *Adv. Colloid Interface Sci.*, **272**, 102009 (2019).
7. M. Ghanbari and M. Salavati-Niasari, *Inorg. Chem.*, **57**, 11443 (2018).
8. Y. Wang, C. Zhu, G. Zuo, Y. Guo, W. Xiao, Y. Dai, J. Kong, X. Xu, Y. Zhou and A. Xie, *Appl. Catal. B: Environ.*, **278**, 119298 (2020).
9. R. Rajendran, K. Varadharajan, V. Jayaraman, B. Singaram and J. Jeyaram, *Appl. Nanosci.*, **8**, 61 (2018).
10. X. Liu, H. Euchner, M. Zarrabeitia, X. Gao, G. A. Elia, A. Groß and S. Passerini, *ACS Energy Lett.*, **5**, 2979 (2020).
11. M. Huang, J. Bian, W. Xiong, C. Huang and R. Zhang, *J. Mater. Chem.*, **6**, 3602 (2018).
12. X. Zhao, Z. Duan and L. Chen, *Ind. Eng. Chem.*, **58**, 10402 (2019).
13. V. Jayaraman, D. Sarkar, R. Rajendran, B. Palanivel, C. Ayappan, M. Chellamuthu and A. Mani, *J. Environ. Manage.*, **247**, 104 (2019).
14. L. Chen, Z. Yang, J. Wu, H. Chen and J. Meng, *Electrochim. Acta*, **330**, 135347 (2020).
15. V. Shrivastava and R. Nagarajan, *Mater. Lett.*, **280**, 128559 (2020).
16. B. Sambandam, V. Soundharrajan, J. Song, S. Kim, J. Jo, P. T. Duong, S. Kim, V. Mathew and J. Kim, *J. Power Sources*, **350**, 80 (2017).
17. D. Xia, S. Xu, W. Wang, D. Wang, M. Wu and F. Gong, *ChemComm.*, **56**, 8043 (2020).
18. Y. Yang, I. C. Infante, B. Dkhil and L. Bellaiche, *C. R. Phys.*, **16**, 193 (2015).

19. C.-C. Zhou, F.-M. Liu, D. Peng, L.-g. Cai and W.-w. Zhong, *J. Alloys Compd.*, **505**, 573 (2010).
20. S. Ninova, M. Strach, R. Buonsanti and U. Aschauer, *J. Chem. Phys.*, **153**, 084704 (2020).
21. J. Sannigrahi, S. Giri and S. Majumdar, *Solid State Commun.*, **228**, 10 (2016).
22. Y. Sun, Z. Ouyang, Y. Xiao, Y. Su, E. Feng, Z. Fu, W. Jin, M. Zbiri, Z. Xia and J. Wang, *Mater. Res. Express.*, **4**, 046101 (2017).
23. S. Jain, B. Sharma, N. Thakur, S. Mishra and T. K. Sarma, *ACS Appl. Nano Mater.*, **3**, 7917 (2020).
24. Y. Liu and Y. Qian, *Front. Chem. China*, **3**, 467 (2008).
25. F. T. Bekena, H. Abdullah, D.-H. Kuo and M. A. Zeleke, *J. Ind. Eng. Chem.*, **78**, 116 (2019).
26. H. Abdullah, N. S. Gultom and D.-H. Kuo, *J. Hazard. Mater.*, **363**, 109 (2019).
27. C. Yang, W. Dong, G. Cui, Y. Zhao, X. Shi, X. Xia, B. Tang and W. Wang, *RSC Adv.*, **7,** 23699 (2017).
28. D. Guerrero-Araque, P. Acevedo-Peña, D. Ramírez-Ortega and R. Gómez, *New J. Chem.*, **41**, 12655 (2017).
29. Z. D. Pozun, S. E. Rodenbusch, E. Keller, K. Tran, W. Tang, K. J. Stevenson and G. Henkelman, *J. Phys. Chem. C.*, **117**, 7598 (2013).
30. S. Wunder, Y. Lu, M. Albrecht and M. Ballauff, *ACS Catal.*, **1**, 908 (2011).
31. D. Newns, *Phys. Rev.*, **178**, 1123 (1969).
32. B. V. Krishna, S. K. Hussain and J. S. Yu, *J. Power Sources*, **506**, 230193 (2021).
33. C. Zheng, B. Jian, J. Zhong and S. Huang, *J. Alloys Compd.*, **934**, 168018 (2023).
34. E. Kamar, K. Qasim and M. Mousa, *Electrochim. Acta*, **430** 141106 (2022).
35. M. Kumar, D. I. Jeong, N. Sarwar, S. Dutta, N. Chauhan, S. A. Han, J. H. Kim and D. H. Yoon, *Appl. Surf. Sci.*, **572**, 151450 (2022).
36. L. Cui, Z. Bai, Z. Li, Z. Liu, H. Ma, X. Chen, K. Lin, J. Hao, Y. Cui and F. Tian, *Appl. Surf. Sci.*, **602**, 154403 (2022).
37. Z. Zhao, X. Wang, S. Wang, Z. Xiao, S. Zhai, J. Ma, X. Dong, H. Sun and Q. An, *Langmuir*, **38**, 11054 (2022).
38. E. M. Sitinjak, I. Masmur, N. V. M. D. Marbun, P. E. Hutajulu, G. Gultom and Y. J. R. a. Sitanggang, *RSC Adv.*, **12**, 16165 (2022).
39. G. Zhang, Y. Wang, F. He, L. He, H. Li and D. Xu, *Catal. Commun.*, **166**, 106454 (2022).